Canadian Science Publishing | Canadian Geotechnical Journal

Shear Resistance Evolution of Geogrid-Aggregate Interfaces under Direct Shear: Insights from 3D DEM Simulations

Journal:	*Canadian Geotechnical Journal*
Manuscript ID	cgj-2023-0531.R1
Manuscript Type:	Article
Date Submitted by the Author:	06-Jan-2024

Complete List of Authors:	Jia, Yafei; Wuhan University Zhang, Jun; Key Laboratory of Highway Construction and Maintenance Technology in Loess Region Ngo, Trung; University of Technology Sydney Zheng, Yewei; Wuhan University

Is the manuscript for consideration in a Special Issue or Collection?:	Not applicable (regular submission)
Keyword:	geogrid, shear band, shear resistance, transverse rib, passive resistance

Shear Resistance Evolution of Geogrid-Aggregate Interfaces under Direct Shear: Insights from 3D DEM Simulations

Yafei Jia[1]; Jun Zhang[2]; Trung Ngo[3]; and Yewei Zheng[4,*]

[1] School of Civil Engineering, Wuhan University, Wuhan, Hubei 430072, China; Email: yafeijia@whu.edu.cn

[2] Shanxi Transportation Technology Research & Development Co., Ltd., Key Laboratory of Highway Construction and Maintenance Technology in Loess Region, Taiyuan 030032, China; Email: zj_sxjt@hotmail.com

[3] School of Civil and Environmental Engineering, Faculty of Engineering and IT, University of Technology Sydney, NSW 2007 Australia. Email: Trung.Ngo@uts.edu.au

*[4] School of Civil Engineering, Wuhan University, Wuhan, Hubei 430072, China; Email: yzheng@whu.edu.cn (*corresponding author)*

***Corresponding author：Yewei Zheng, Wuhan University, E-mail: yzheng@whu.edu.cn**

Abstract: This paper presents a mesoscopic evaluation of the shear resistance evolution of geogrid-aggregate interfaces subjected to direct shear loading. A three-dimensional discrete element method (DEM) model was developed based on experimental data. The tensile response of geogrid were simulated through a series of calibration tests. Aggregate with complex particle shapes were simulated to accurately capture the interlocking effect among aggregates based on the real particle surface. The individual shear resistance components were quantified based on particle displacement field and contact distribution characteristics. The influences of aperture-aggregate size ratio and geogrid stiffness on the shear resistance components are discussed. The results indicate that the peak value of shear resistance component follows a descending order from frictional resistance of aggregate, to passive resistance of transverse rib, and to geogrid-aggregate interface frictional resistance. During the shear process, the frictional resistance of aggregate becomes active first, followed by the geogrid-aggregate interface frictional resistance, and then the development of passive resistance of transverse ribs starts with a certain lag. Optimizing the geogrid-aggregate size ratio and utilizing geogrids with higher rib stiffness could enhance the passive resistance of transverse ribs but would not significantly affect the geogrid-aggregate interface frictional resistance and frictional resistance of aggregate.

Keywords: geogrid, direct shear test, shear band, shear resistance, transverse rib, passive resistance.

Résumé : Cet article présente une évaluation mésoscopique de l'évolution de la résistance au cisaillement des interfaces géogrille-granulats soumises à une charge de cisaillement direct. Un modèle de méthode des éléments discrets (MED) tridimensionnel entièrement calibré a été développé en se basant sur des données expérimentales. La réponse à la traction et le comportement en déformation de la géogrille ont été simulés par le biais d'une série de tests de calibration. Les granulats aux formes de particules complexes ont été simulés afin de capturer avec précision l'effet d'interblocage entre les granulats basé sur la surface réelle des particules. Les composantes individuelles de résistance au cisaillement ont été quantifiées en se basant sur le champ de déplacement des particules et les caractéristiques de distribution des contacts. Les influences du rapport de taille entre l'ouverture et les granulats ainsi que de la rigidité de la géogrille sur les composantes de résistance au cisaillement sont discutées. Les résultats indiquent que la valeur maximale de la composante de résistance au cisaillement suit un ordre décroissant de la résistance au frottement des agrégats à la résistance passive des nervures transversales, puis à la résistance au frottement de l'interface géogrille-agrégat. Au cours du cisaillement, la résistance au frottement des agrégats s'active en premier, suivie de la résistance au frottement de l'interface géogrille-agrégat, puis le développement de la résistance passive des nervures transversales commence avec un certain retard. L'optimisation du rapport taille des ouvertures/taille des agrégats et l'utilisation de géogrilles à nervures plus rigides pourraient améliorer la résistance passive des nervures transversales, mais n'affecteraient pas de manière significative la résistance au frottement de l'interface géogrille-agrégat et la résistance au frottement des agrégats.

Mots-clés : Géogrille, Essai de cisaillement direct, Bande de cisaillement, Résistance au cisaillement, Nervure transversal, Résistance passive.

1. Introduction

Geogrids are widely used in various soil reinforcement projects in the field of geotechnical engineering, providing feasible solutions to land utilization and structural stability issues (Jia et al., 2021; Ke et al., 2021; Liu et al., 2007; Yang et al., 2012; Zhang et al., 2022). In the design of geogrid-reinforced soil structures, the shear behavior of geogrid-soil interfaces is a crucial consideration, as it significantly influences the performance and stability of geosynthetic reinforced soil (GRS) structures (Jewell et al., 1985). Hence, the interaction mechanism between the geogrid and soil is of great significance in understanding the behavior of GRS structures.

The characterization of geogrid-soil interfaces is vital in enhancing the understanding of geogrid-soil interaction. Various testing approaches have been developed for this purpose, including pull-out tests, direct shear tests, in-soil tensile tests, and ramp tests (Palmeira, 2009). Among them, pull-out tests and direct shear tests have been widely adopted to study the conditions and broad applicability(Abdelrahman et al., 2008; Alfaro et al., 1995; Ezzein and Bathurst, 2014; Liu et al., 2009b; Lopes and Ladeira, 1996). The interaction between the geogrid and soil in pull-out tests is associated with interface frictional resistance and rib-bearing resistance (i.e., passive resistance of transverse ribs) of the geogrid. Previous studies have been conducted for quantitative evaluations of the rib-bearing resistance of geogrids, revealing that transverse ribs contribute approximately 75% to 90% of the total pull-out resistance (Cardile et al., 2017; Moraci and Gioffrè, 2006; Palmeira and Milligan, 1989). This emphasizes the vital role of geogrid’s transverse ribs in the shear resistance of the geogrid-soil interface.

Nevertheless, few studies have focused on the quantitative evolution of individual shear resistance components at the geogrid-aggregate interface under direct shear conditions. Liu et al. (2009a) conducted a series of direct shear tests on geogrid-soil interfaces, studying the interaction at the geogrid-soil interface during direct shear, which comprises soil-soil frictional resistance, geogrid surface-soil frictional resistance, and passive resistance of geogrid transverse ribs. Presently, the evaluation of passive resistance of transverse ribs is primarily based on a comparison of the peak shear strength between the reinforced and unreinforced specimens, along with the ratio of the geogrid opening area to the area of the reinforced plane (Jia et al., 2023; Liu et al., 2009a). However, the evolution of individual components contributing to the total shear resistance during the shear process remains unclear, and there is a need for investigating the evolution of passive resistance of transverse ribs during the shearing process. Consequently, the interaction mechanism of geogrid and aggregates in the direct shear mode has not been fully revealed, necessitating a mesoscopic perspective to comprehend the interface interaction and clarify the underlying reinforcement mechanism.

Most experimental studies have focused on the macroscopic mechanism of geogrid-soil interaction (Ferreira et al., 2015; Liu et al., 2016; Sweta and Hussaini, 2018; Wang et al., 2019). However, the factors influencing the interaction between the geogrid ribs and soil particles can be divided into two categories (Zhou et al., 2012). One is related to the micro behavior of the soil and the geogrid, including grain size, particle shape of soil, and local deformation of the geogrid. The other relates to macro boundary conditions, specimen size, and stress state. While experimental studies have provided significant insights, most conventional testing methods have limitations in revealing microscale interactions at the geogrid-aggregate interface, such as interlocking and contact force evolution between individual aggregates. Although non-intrusive measurements, such as high-resolution digital cameras (Abdi and Mirzaeifar, 2017; Zhou et al., 2012) and transparent soil laser-assisted imaging (Peng and Zornberg, 2019), have been adopted in laboratory to study the micro-mechanisms interaction between the geogrid and aggregates, the results are limited to capturing deformation patterns. Quantifying and tracking the geogrid-aggregates interlocking behavior and the evolution of individual shear resistance components during the shear process remains challenging. Therefore, it is necessary to utilize the Discrete Element Method (DEM) to simulate and track the interaction between the geogrid and soil particles from a micromechanical perspective.

DEM has been widely used to investigate the meso-scale behavior, such as interlocking and sliding between soil particles, in studies on soil-structure interface behavior (Chen et al., 2018; Grabowski et al., 2021; Jia et al., 2023; McDowell et al., 2006; Miao et al., 2020; Ngo et al., 2014; Wang et al., 2022; Wang and Yin, 2022). Previous research has indicated two crucial factors that should not be overlooked in the interaction of geogrid-soil interfaces: the particle shape of aggregates (Ferellec and McDowell, 2010; Gao and Meguid, 2018; Miao et al., 2017; Stahl et al., 2014; Tutumluer et al., 2012; Zhou et al., 2018), which directly affects the relative movement and rotation of particles, and the flexural stiffness of geogrid (Feng and Wang, 2023; Ferellec and McDowell, 2012; Jia et al., 2023), which directly influences the deformation mode of geogrid. Therefore, accurately reproducing the particle shape of soils and the local deformation response of geogrids is crucial in numerical simulations.

In this study, direct shear tests are conducted on the geogrid-aggregate interfaces and the corresponding DEM models are developed to quantitatively evaluate the evolution of individual shear resistance components subjected to direct shear loading. The influences of aggregate shape and geogrid flexural stiffness are considered. The passive resistance of transverse ribs is quantified based on the distribution of shear bands and the evolution of contact forces. The results of this study provide a better understanding of the interaction mechanism between the geogrid and aggregates from a meso-mechanical perspective, which is of significance for the design of GRS structures.

2. DEM Model and Parameter Calibration

The DEM model of geogrid-aggregate interface shear was developed using PFC3D. DEM modeling procedures of geogrid and aggregate are introduced, and the corresponding calibration of parameters is established based on the experimental results.

2.1 Geogrid

The present study employed a typical polypropylene biaxial geogrid as a reinforcement. This geogrid has an average joint thickness of 5.0 mm and rib thickness of 3.5 mm. The center-to-center distance between two adjacent joints is 40 mm, and the width of the geogrid ribs varies from 8 mm to 4 mm between these joints. The geometric characteristics of geogrid were simulated in the DEM model using bonded sphere strings, with particle sizes ranging from 1.5 mm to 3 mm. The contact between the spheres was governed by the linear parallel bond contact model, which allows for the transmission of bending and tensile forces. This contact model has also been extensively utilized to simulate the tensile behavior of geogrids accurately (Chen et al., 2012; Feng and Wang, 2023; Ferellec and McDowell, 2012; Ngo et al., 2014; Stahl et al., 2014). For per timestep, the increment of normal and tangential forces $\Delta\bar{F}_{n,s}$, bending moments $\Delta\bar{M}_b$, and twisting moments $\Delta\bar{M}_t$ within the parallel bond can be mathematically described as follows:

$$\Delta\bar{F}_{n,s} = \bar{A}\Delta U_{n,s}\bar{k}_{n,s} \tag{1}$$

$$\Delta\bar{M}_b = I\Delta\theta_b\bar{k}_n \tag{2}$$

$$\Delta\bar{M}_t = J\Delta\theta_t\bar{k}_s \tag{3}$$

Where, $\Delta U_{n,s}$, $\Delta\theta_b$, and $\Delta\theta_t$ are the increment of relative normal and shear displacement, the increment of relative bend rotation, and the increment of relative twist rotation, respectively; $\bar{k}_{n,s}$ is the normal and shear stiffness of parallel bond; $\bar{A}$, I and J are the parallel bond cross-section area, the moment of inertia of the parallel bond cross section and the polar moment of inertia of the parallel bond cross-section, respectively, which are calculated as:

$$\bar{A} = \pi\bar{R}^2 \tag{4}$$

$$I = \frac{1}{4}\pi R^4 \tag{5}$$

$$J = \frac{1}{2}\pi R^4 \tag{6}$$

where $\bar{R} = \min(R_1, R_2)$ is the radius of the smaller of the two pieces in contact with each other. The effective modulus $\bar{E}^*$ and stiffness ratio $\bar{\kappa}^*$ of parallel bond, as input parameters related to Young's modulus (tension) and Poisson's ratio, can be calculated by the following formula:

$$\bar{E}^* = \bar{k}_n L \tag{7}$$

$$\kappa^* = \frac{\bar{k}_n}{\bar{k}_S} \tag{8}$$

where $L = R_1 + R_2$ is the contact length, which can be represented as the sum of the radius of two pieces in contact with each other.

The calibration of contact parameters for tensile properties primarily relies on the experimental results of single rib tensile tests. As shown in Fig. 1, tensile tests were conducted along both the machine direction (MD) and the cross-machine direction (CMD) of the geogrid. In general, the tensile test results from the experiments and simulations are in good agreement for both the MD and CMD. During the direct shear test of geogrid-aggregate interfaces, the local strain of geogrid with typical stiffness did not exceed 5% (Jia et al., 2023). Within this range of strain, the stress-strain relationship of the geogrid used in this study is nearly linear. For the subsequent simulations, high values were assigned to the normal and shear strength of the parallel bond to prevent failure (i.e., rupture), as this study primarily focuses on the interlocking behavior between the geogrid and aggregates under typical normal stresses. Overall, the numerical simulation results are in good agreement with the experimental results.

To replicate the deformation mode of geogrid in the numerical simulations accurately, it is crucial to consider the aperture stability and bending resistance of geogrid. The two-aperture extension tests were conducted, as shown in Fig. 2, to calibrate the deformation behavior of geogrid model. The observed deformations of geogrid include upward buckling of the middle transverse rib, tension, and outward rotation of the longitudinal ribs on both sides. To quantify these deformations, the flexible buckling height (h_f) of the middle section of the transverse rib and the distance, d, between the two joints connecting the transverse rib were measured. With a tensile force F_t = 0.25 kN, the test yielded h_f/d = 2.16. In Fig. 2 (b), the distribution of contact tension within the numerical model produces the value of h_f/d = 2.07, which demonstrates an excellent agreement with the experimental results. Consequently, the model parameters employed in this study can effectively capture the tensile response and deformation behavior of geogrid. Table 1 provides an overview of the calibrated geogrid model parameters.

2.2 Aggregate

The tests in this study utilized limestone as the aggregate, which possesses angular characteristics. The comparison of particle size distribution of the gravel from the experiments and DEM simulations is presented in Fig. 3(a). Previous experimental and simulation studies have demonstrated that particle shape significantly influences the interlocking among particles (Liu et al., 2021; Wang et al., 2021; Ying et al., 2021; Zhou et al., 2018). In the DEM simulations, an aggregate modeling method based on the real particle surface was employed to accurately capture the interlocking effect among aggregates. The aggregate model employs overlapping spheres to replicate the shape of actual irregular particles using 'clump' logic (Ferellec and McDowell, 2010; Ferellec and McDowell, 2012). The surface of a real particle is first captured as a cloud of points in 3D space using scanning techniques. Spheres are then grown from random points on this surface, expanding normally to the maximum extent possible inside the particle volume without penetrating the surface boundary. Each sphere expands as much as possible to fill the interior volume. The more spheres used, the better the resolution of the particle shape. This allows complex realistic particle shapes to be generated for DEM simulations by filling the scanned volume with optimized overlapping spheres, which helps to mimic the actual particle shape. It should be noted that the aggregate model in this study cannot simulate particle breakage. The normal and shear stresses involved in this study are much smaller than the breakage strength of limestone (typically greater than 5 MPa) (Feng et al., 2022; Wang et al., 2023). Therefore, the influence of particle breakage is ignored in this study.

To ensure accurate particle dynamics and prevent incorrect inertia caused by uneven mass distribution due to sphere overlap, this study utilizes a calculation method that assumes a homogeneous polyhedron. The centroid and inertia tensor of the polyhedron are computed accordingly (Mirtich, 1996). The linear contact model in DEM was adopted for the contact between particles. This model is widely used in simulating cohesionless materials and has been proven to be highly reliable in capturing their behavior (McDowell et al., 2006; Ngo et al., 2014; Stahl et al., 2014; Wang et al., 2022; Wang et al., 2014; Zhou et al., 2018). The linear contact model is dominated by a linear-elastic spring contact law. The incremental normal and shear contact force, $\Delta F_{n,s}$, and friction strength update can be calculated as:

$$\Delta F_{n,s} = \Delta U_{n,s} k_{n,s} \tag{9}$$

$$F_s = \mu F_n \tag{10}$$

where $\Delta U_{n,s}$ is the incremental normal and shear displacement; $k_{n,s}$ is the normal and shear stiffness; μ is the interparticle friction coefficient. The effective modulus E^* and stiffness ratio K^* of linear contact can be calculated:

$$E^* = \frac{k_n L}{\Pi R_{\min}^2} \tag{11}$$

$$K^* = \frac{k_n}{k_s} \tag{12}$$

where L and $R_{\min}$ are the contact length and the smaller radius of the two pieces in contact, respectively.

Furthermore, to ensure computational efficiency, the influence of particle shape is assessed based on the peak shear strength observed in the direct shear test (detailed information on the direct shear test process is provided later). The approximation effect of particle shape is quantitatively evaluated using a volume error, E_V, which can be expressed as follows (Katagiri, 2019):

$$E_V = \frac{|V_S - V_C|}{V_S} \tag{13}$$

where V_S represents the volume of the closed three-dimensional polyhedron representing the particle surface, and V_C represents the volume of the clump particle.

Fig. 3(b) compares the simulation results and the direct shear test results for four different types of particles, each characterized by a different volume error (E_{Vi}). To balance the computational efficiency and accuracy, the volume error selected for the aggregate particles in this study is E_{V3} = 0.087.

Fig. 4 shows the direct shear test results for aggregates obtained from the experiments and the DEM simulations. The comparison between these results demonstrates a reasonable agreement, indicating that the DEM model can capture the evolution of shear strength of the aggregate. This agreement further validates the accuracy and reliability of the DEM model. The calibrated parameters of the aggregates adopted in the current DEM analysis are summarized in Table 2.

2.3 Geogrid-aggregate interface direct shear tests

The direct shear test apparatus is presented in Fig. 5. It consists of upper and lower shear boxes constructed from steel plates, providing rigid boundary conditions. The upper and lower shear boxes both have a height of H = 200 mm and a width of W = 300 mm. The length of the upper shear box along the shear direction is L= 300 mm, while the length of the lower shear box is L_l = 360 mm. The larger area of the lower shear box can ensure a constant contact area during the shearing process. A vertical actuator was connected to the top of the upper shear box to apply constant normal stress. A horizontal actuator was utilized to apply shear stress on the lower shear box at a constant rate. The geogrid specimen was fixed to the front edge of the lower shear box using clamping blocks and bolts. The longitudinal rib of the geogrid aligned with the shear direction, while the transverse rib was perpendicular to the shear direction. According to ASTM D 5321, the geogrid extended with a sufficient distance along the relative movement direction of the upper shear box to enable clamping to the lower shear box. During specimen preparation, the weight of soil in both the upper and lower shear boxes was carefully controlled to ensure a consistent compacted soil density of ρ_c = 1600.5 kg/m^3. A constant shear rate of v_s = 1 mm/min was applied to the lower shear box until the shear displacement reached 30 mm. Tests were conducted under four different normal stresses of σ_n = 50 kPa, 100 kPa, 150 kPa, and 200 kPa.

Fig. 6 shows the DEM model of the direct shear test. The upper and lower shear boxes were constructed with rigid friction-free walls, providing appropriate boundary conditions. The initial dimensions of the simulated shear boxes aligned with those of the laboratory tests, while the initial height (H_{ini}) was set to 400 mm to ensure an adequate number of particles generated within the shear box and compacted to achieve the target density. Through iterative adjustments, it was determined that setting the initial porosity to 0.55 yielded an aggregate particle height (H) after final compaction that closely matched the experimental conditions. The geogrid model, as shown in Fig. 6(a), was implemented to maintain the alignment of longitudinal ribs along the shear direction. The geogrid particles were clamped and securely affixed to the lower shear box. Subsequently, a constant target normal stress was applied to the top of the shear box. Finally, a constant shear rate was applied to the lower shear box.

The linear contact model was employed to simulate the interaction between the geogrid and aggregate particles. Fig. 7 shows the comparison between the results of experiments and DEM simulations. Before reaching the peak shear stress, the DEM simulations display a higher stiffness compared to the experimental data. This discrepancy could be attributed to the difference in the specimen preparation technique. Previous studies have highlighted that uniformly compacted DEM specimens often exhibit non-physical load-deformation response at low strain levels, which could explain the stiffer response before attaining the peak stress in the DEM simulations (Feng et al., 2018; Thornton, 2000). Moreover, the disparity in post-peak strength between the DEM simulations and experiments under the normal stress σ_n = 200 kPa could be due to the localized instability. The local instability of the specimen can be attributed to the relative slip and rotation of coarse particles during the shearing process, which can result in the failure and reconstruction of inter-particle interlocking. In general, the DEM simulation results agree with the experimental results. It indicates that the DEM model developed in this study can effectively capture the nonlinear development of shear stress with increasing shear displacement and accurately represent the shear behavior of geogrid-aggregate interfaces. The calibrated parameters of geogrid-aggregate interface in the DEM simulations are summarized in Table 3.

3. Results and Discussions

3.1 Interface shear resistance

A dimensionless parameter, known as the shear strength coefficient, α, is employed to quantify the reinforcement effect of geogrid-aggregate interfaces (Liu et al., 2009a; Tatlisoz et al., 1998). The value α is determined as follows:

$$\alpha = \frac{\tau_{s-g}}{\tau_s} \tag{14}$$

where τ_{s-g} and τ_s represent the peak shear strengths of the geogrid-aggregate interface and the unreinforced aggregates, respectively. Fig. 8(a) shows the comparison of the shear strength coefficient (α) obtained from the experiments and DEM simulations. The experimental and simulated values of α are greater than 1.0 and generally close to each other. This indicates that the geogrid can effectively enhance the shear strength of aggregates and further validate the effectiveness of the DEM model.

Fig. 8(b) presents the corresponding shear displacements at the peak shear strength obtained from the direct shear tests. The shaded area illustrates the difference between the corresponding shear displacements of reinforced and unreinforced specimens. Both the experimental and simulated results consistently demonstrate that the shear displacements at the geogrid-aggregate interfaces are significantly larger than those of the unreinforced specimens when the shear stress reaches the peak value. Previous studies have attempted to develop quantitative evaluation methods for individual shear resistance components (Jia et al., 2023; Liu et al., 2009a; Liu et al., 2009b). One such approximate method, proposed by Liu et al. (2009a), involves allocating the total peak shear resistance based on the ratio of the surface area of the geogrid to the total shear plane, and the ratio of the opening area of the geogrid to the total shear plane. This assumes that the peak values of each resistance component occur simultaneously. However, the data presented in Fig. 8(b) indicates that the peak values of each component of the geogrid-aggregate interface shear resistance may not be synchronized. For instance, the differences in shear displacement mobilized at peak shear stress between the reinforced and unreinforced specimens under 50 kPa normal stress obtained from experiment and DEM simulation were approximately 6.5 mm and 6.3 mm, respectively. This indicates that the different shear resistance components may have different mechanisms for the mobilization of shear strength. Hence, it becomes crucial to accurately quantify the evolution process of each shear resistance component, especially the passive resistance provided by the transverse ribs, to investigate the reinforcement mechanism of geogrid-aggregate interfaces.

3.2 Individual shear resistance components

As shown in Fig. 9, the total shear resistance of the geogrid-aggregate interface can be divided into three components: (i) internal frictional resistance, FR_s, which originates from the internal friction provided by the contact among the particles within the aperture. (ii) geogrid-aggregate interface frictional resistance, FR_{gs}, which arises from the frictional resistance between the geogrid surface and particles. (iii) passive resistance, PR_g, which is attributed to the resistance exerted on the inner side of the transverse ribs resulting from the transverse rib-aggregate interaction.

The interaction between the geogrid and aggregates at the geogrid-aggregate interface can be better understood from a meso-perspective by examining the contact force distribution. As an example, for the simulation with normal stress σ_n = 50 kPa, Fig. 10 presents the contact force distribution around a representative geogrid aperture, simulated at different shear displacements. The ribs of geogrid serve as tension members, experiencing internal tensile contact forces (geogrid-geogrid contacts). Conversely, the aggregate-geogrid contacts and aggregate-aggregate contacts are characterized by pressure-bearing contacts. These contacts collectively form a force transmission network known as the contact force chains. As the shear displacement increases, the contact directions adjust accordingly to adapt to the new stress conditions. The passive resistance provided by geogrid ribs can be explained from a meso-perspective as follows: a portion of the aggregates is trapped within the aperture and exerts forces on the inner side of the ribs through contacts. The transverse ribs of geogrid actively resist the relative movement of aggregates along the shear direction, thereby influencing the displacement and contact state of particles. The interaction between the geogrid and aggregates involves a complex mechanism, including the relative motion of particles, the evolution of contact directions, and contact forces. The contribution of each shear resistance component to the total shear strength and its evolution by considering the relative movement and contact evolution of particles will be elaborated in the following sections.

3.3 Geogrid deformations

Fig. 11 presents the comparison of geogrid deformations between the experiment and DEM simulation under the normal stress of σ_n = 50 kPa. Both the experiment and DEM simulation reveal similar deformation patterns: the longitudinal ribs along the shear direction have minimal bending deformations, while the transverse ribs (perpendicular to the shear direction) exhibit obvious flexible bending deformations, which emphasizes the crucial role of passive bearing resistance of transverse ribs in direct shear tests. The consistency between the experimental and simulated deformations further validates the effectiveness of DEM model. It is important to note that the geogrid deformations observed in the experiment from Fig. 11(a) may be slightly smaller than the actual geogrid deformations after shear. This discrepancy arises because the shear force and the upper shear box were removed before taking the photo for observation, leading to partial recovery of the elastic deformations of geogrid. Fig. 11(b) also shows slices of aggregate particles at the interface after direct shear. A prominent observation is that the aggregate particles subjected to shear at the geogrid-aggregate interface consistently tend to move along the shear direction. The restraining effect of geogrid on the aggregate particles primarily manifests in the particles being obstructed in front of the transverse ribs.

3.4 Shear band

In the direct shear tests of geogrid-aggregate interfaces, the shear plane is located along the upper surface of the geogrid. Consequently, the deformation primarily occurs within a narrow region known as the shear band near the geogrid surface. Identifying the shear band of the geogrid-aggregate interface and quantifying its thickness based on particle kinematics can aid in determining the interaction region. Fig. 12(a) presents the horizontal displacements of the aggregates under normal stress of σ_n = 50 kPa (negative values denoting displacements along the shear direction). Jing et al. (2018) proposed a method to quantitatively assess the thickness of the local shear band by utilizing the inflection point of the δ_x-d curve, where δ_x and d are the displacement of aggregates in the x-axis direction and the depth of aggregate particles, respectively. To determine the thickness of the shear bands, the average displacement component of particles in the shear direction (x-axis) is first calculated by averaging the displacement field. Subsequently, a smooth curve $f(d)$ is obtained through spline interpolation, representing the relationship between the displacement in the x-axis direction (δ_x) and the thickness of the local zone. The first derivative $f'(d)$ and the second derivative $f''(d)$ are then computed using the finite difference method. Finally, the curvature κ can be calculated as follows:

$$\kappa = \frac{|f'(d)|}{(1+f'(d)^2)^{3/2}} \tag{15}$$

As suggested by Jing et al. (2018), the curvature κ = 0.02 can be employed as the criterion to define the boundary of the local shear band. In direct shear tests, the two boundaries of the shear band are above and below the geogrid layer located in the upper and lower shear boxes, respectively. The thickness of the upper and lower shear bands can be defined as the distance from the corresponding boundary (upper or lower) of the shear band to the upper surface of the geogrid. Fig. 12(a) shows that the thickness of the upper shear band is significantly thicker than that of the lower shear band. For instance, at a normal stress of σ_n = 50 kPa, the thickness of the upper shear band is 42.6 mm, while the thickness of the lower shear band is 15.1 mm. This indicates that the relative motion of particles within the upper shear band is more pronounced. This can be attributed to two main factors: Firstly, the servo normal stress is achieved through displacement control by the actuator placed at the top of the upper shear box. As a result, if there is a tendency for shear expansion at the interface, this servo mechanism enables the particles to move upward rather than downward; Secondly, the shear interface is located on the upper surface of the geogrid rather than the lower surface, which influences the intensity of particle motion within the shear band. Similar observations were also reported by Feng and Wang (2023).

Fig. 12(b) displays the variations in shear band thickness under different normal stresses. In general, as the normal stress increases, the boundaries of both the upper and lower shear bands move downward, while the total thickness of the shear band (the sum of the thicknesses of the upper and lower shear bands) remains near constant at approximately $3.4D_{50}$ (D_{50} is the average particle size). This observation indicates that higher normal stress prevents the upward expansion of the shear zone but promotes its downward progression. Several studies have also demonstrated that under higher normal stresses, aggregate particles tend to be tightly compressed and interlocked, resulting in less macroscopic volume dilatancy (Ferreira et al., 2015; Wang et al., 2021).

3.5 Contact force distribution

The distribution of contact forces between particles can provide insights into the load transfer mechanism at the geogrid-aggregate interface. In this study, the shear direction is defined as the negative direction along the *x*-axis, indicating that the shear resistance acts in the *x*-axis direction, while the vertical normal stress is defined as the negative direction along the *z*-axis. Thus, the contact forces can be projected onto the *x-o-z* plane to quantify the distribution. Rothenburg and Bathurst (1989) proved that the distribution of the contact normal $C(\theta)$ and the normal contact force $f(\theta)$ between particles can be approximated using second-order Fourier series:

$$C(\theta) = \frac{1}{2\pi}[1 + a_c \cos 2(\theta - \theta_c)] \tag{16}$$

$$f(\theta) = f_0[1 + a_n \cos 2(\theta - \theta_n)] \tag{17}$$

where a_c and a_n are the anisotropy coefficients of the contact normal and normal contact forces, respectively; θ_c and θ_n are the principal directions of contact normal and normal contact force distribution, respectively; f_0 is the average normal contact force. Fig. 13(a) presents the contact force distribution in the geogrid-aggregate interface shear specimen at the peak shear stress under σ_n = 50 kPa. The thickness of lines represents the magnitude of force chains. Some localized voids in the force chains near the transverse rib of geogrid indicate that the relative motion of particles caused by shear is influenced by the transverse rib. The sparseness of force chains at the end of the upper shear box (away from the clamped end of geogrid) indicates a local reduction in normal stress, which is consistent with the results reported by Teixeira et al. (2007). Furthermore, the direction of contact force in the upper shear band exhibits the most pronounced deflection. To further analyze the contact forces in this region, the normal and tangential contact forces between aggregates are counted and analyzed using Fourier series approximation (FSA) fitting. Fig. 13(b) and 13(c) show the FSA fitting results for the contact normal and normal contact forces, respectively. The principal direction of the contact normal describes the relative position information of particles, while the principal direction of the normal contact force distribution describes the primary load information borne by the current force chain of microstructure. The principal direction of the contact normal is $\theta_c = 35°$, and the principal direction of the normal contact force distribution is $\theta_n = 48°$. Additionally, the angle between the normal contact direction and the shear direction is represented as $\alpha_c = \pi/2 - \theta_c$, which can be used to determine whether the contact contributes to the passive resistance of transverse ribs.

Fig. 14 shows the variations of θ_c and θ_n for specimens captured at the peak shear stress under different normal stresses. The trend of θ_c and θ_n changing with normal stress is consistent. The principal directions of contact normal fluctuate between 35° and 37°. The principal directions of the normal contact force are always greater than those of the contact normal, ranging between 48° and 53°.

4. Determination of Individual Shear Resistance Components

Based on the previous analysis, the contact between the geogrid and aggregates, contributing to the passive resistance of transverse ribs, must satisfy two conditions: One is that the contact point should be between the transverse rib and aggregate particle; the other is that the contact position should be located at the inner edge of the transverse rib, and the angle between the projection of the contact normal direction (from the geogrid to the aggregate particles) in the *x-o-z* plane and the shear direction should be less than α_c, as shown in Fig. 15.

Once these contacts are identified, the passive resistance of transverse ribs, PR_g, during shearing can be calculated as:

$$PR_g = -\sum_{a_{PR} \le a_c} f_x^{(gt-s)} \tag{18}$$

where f_{gt-s} is the x-direction component of the contact force for transverse rib-aggregate contact. By subtracting the passive resistance of transverse ribs from the total geogrid resistance, the geogrid-aggregate interface frictional resistance (FR_{gs}) on the geogrid-aggregate interface can be determined:

$$FR_{gs} = \sum f_{xi} - PR_g \tag{19}$$

where f_x represents the component of the contact force in the x-direction between the clamped part of the geogrid and the rest of the geogrid, as shown in Fig. 15(b). Then, the internal frictional resistance of aggregates (FR_s) is determined by subtracting the total geogrid resistance from the total shear resistance. Moreover, quantifying the various shear resistance components at the geogrid-aggregate interface make it possible to gain insights into the evolutions of individual components. This provides a comprehensive understanding of the interaction between the geogrid and aggregates, shedding light on the reinforcement mechanism.

Fig. 16 presents the evolution of shear resistance components as shear displacement progresses under different normal stresses. The peak value of each shear resistance component follows a descending order from frictional resistance of aggregate (FR_s), to passive resistance of transverse ribs (PR_{gs}), and to geogrid-aggregate interface frictional resistance (FR_{gs}). During the shear process, with increasing shear displacement, the first occurrence of peak shear resistance corresponds to the geogrid-aggregate interface frictional resistance, followed by the frictional resistance of aggregate, and the passive resistance of transverse ribs.

Take the specimen under σ_n = 50 kPa as an example to elucidate the evolution process of each shear resistance component, as shown in Fig. 16(a). Initially, the frictional resistance between aggregates becomes active, succeeded by the geogrid-aggregate interface frictional resistance. However, the development of passive resistance of transverse ribs exhibits a certain lag, particularly during the early stages of shear. Similar trends are observed under different normal stresses. Additionally, each shear resistance component significantly increases with the increase of normal stress. For instance, under normal stresses of σ_n = 50 kPa, 100 kPa, 150 kPa, and 200 kPa, the peak values of the passive resistance of transverse ribs are 1.72 kN, 2.01 kN, 2.63 kN, and 3.31 kN, respectively. Notably, the frictional resistance of aggregate component demonstrates the most substantial increase as the normal stress increases, as the soil strength significantly depends on the normal stress for granular soils.

Fig. 17 shows the evolution of the contribution (i.e., the proportion concerning the total shear resistance) of each shear resistance component, represented by C_{PRG}, C_{FRG}, and C_{FRS}, which denote the contribution of passive resistance of transverse ribs, geogrid-aggregate interface frictional resistance, and frictional resistance of aggregates, respectively. Based on the peak total shear stress, the shear displacement is divided into two stages: pre-peak and post-peak. Prior to reaching the peak total shear stress, the contribution of passive resistance of transverse ribs continues to increase, while the contribution of frictional resistance of aggregate fluctuates and decreases. The contribution of geogrid-aggregate interface frictional resistance initially increases and subsequently decreases. Interestingly, during the initial shear stage, the contribution of transverse rib passive resistance is lower than that of the geogrid-aggregate interface frictional resistance. However, with further increasing shear displacement, the contribution of transverse rib passive resistance gradually increases and surpasses the contribution of the geogrid-aggregate interface frictional resistance, indicating the attainment of a relatively strong interlocking state in the geogrid-aggregate system. When the total shear resistance reaches its peak under each normal stress, the contribution of the passive resistance of transverse ribs ranges from 16.7% to 22.8%. Notably, the maximum contribution of the passive resistance of transverse ribs consistently occurs after the peak total shear stress. In this study, the maximum contribution of the passive resistance of transverse ribs reached 43.5%, as shown in Fig. 17(a). In the post-peak stage of the total shear stress, the contribution of transverse rib passive resistance continues to increase until it reaches the peak and then fluctuates. This indicates that the passive resistance of transverse ribs can be maintained under relatively large shear displacements. Overall, during the entire shear process, the contribution of frictional resistance of aggregate exceeds the other two shear resistance components. This is attributed to the large opening area of the geogrid aperture, which leads to more aggregate-aggregate contacts and interactions contributing to shear resistance compared to aggregate-geogrid contacts.

5. Influence of Aperture-aggregate Size Ratio

The relationship between aperture size and aggregate size has been identified as a significant factor influencing the shear strength of geogrid-aggregate interfaces (Brown et al., 2007; Liu et al., 2022; Miao et al., 2020; Wang et al., 2016). This relationship is commonly evaluated using the aperture-aggregate ratio, A_s/D_{50}, defined as the ratio of the geogrid aperture size (A_s) to the average particle size of aggregate (D_{50}). In the geogrid-reinforced aggregate structures, typical geogrid aperture sizes range between 15 mm and 65 mm (Indraratna et al., 2013; Liu et al., 2009a). To investigate the influence of aperture-aggregate ratio on the passive resistance of transverse ribs, geogrid models with aperture sizes of 28 mm, 40 mm, and 56 mm (corresponding to aperture-aggregate ratios of A_s/D_{50} = 1.67, 2.38, and 3.33, respectively) were utilized for geogrid-aggregate interface direct shear tests. All these simulations were conducted under a normal stress σ_n = 50 kPa while keeping the micro-contact parameters consistent with the previously calibrated values.

As shown in Fig. 18(a), the specimen with A_s/D_{50} = 2.38 exhibits the highest total shear strength. This is because this aperture-aggregate ratio promotes interlocking between the coarse aggregate-geogrid apertures. Fig. 18(b)-(d) presents the evolution curves of each shear resistance component with shear displacement for specimens with different A_s/D_{50}. The data indicate that the passive resistance of transverse ribs in the specimen with A_s/D_{50} = 2.38 is significantly greater than those of the other specimens. In contrast, the geogrid-aggregate interface frictional resistance and the frictional resistance of aggregate are similar for all specimens. The results demonstrate the significance of the passive resistance of transverse ribs in enhancing the overall shear strength.

6. Influence of Geogrid Rib Stiffness

The secant stiffness at 2% strain of the geogrid, $J_{2\%}$, can be determined through geogrid tensile tests and is considered as a crucial factor influencing the shear strength of geogrid-aggregate interfaces. The tensile stiffness values of several typical geogrids used in field projects ranging from 330 kN/m to 1185 kN/m (Jia et al., 2021; Jiang et al., 2016; Yang et al., 2012). To investigate the influence of geogrid stiffness on the passive resistance of transverse ribs, several additional geogrid numerical models were developed. The secant stiffness was set as $J_{2\%}$ = 330 kN/m, 660 kN/m, and 990 kN/m, respectively. It is noteworthy that, compared to the specimen with $J_{2\%}$ = 330 kN/m, the normal stiffness of parallel bond, $\bar{k}_n$, in the other models was uniformly scaled, ensuring that the stiffness ratio between the transverse and longitudinal ribs remained constant.

Fig. 19 presents a comparison of simulation results from direct shear tests for geogrids having three different secant stiffnesses. The results reveal that the peak shear stress increases with the increase of geogrid stiffness, as expected. When examining the evolution of shear resistance components, it is observed that increasing geogrid stiffness has minimal effect on frictional resistance of aggregate (FR_s) and geogrid-aggregate interface frictional resistance (FR_g) but significantly influences the passive resistance of transverse ribs (PR_g). Additionally, at relatively small shear displacements (< 2.5 mm), the passive resistance of transverse ribs remains relatively low but rapidly increases as the shear displacement increases (Fig. 19(b)). This behavior can be attributed to the interaction mechanism between the transverse ribs of geogrid and aggregate, which leads to flexible deformation of transverse ribs (Fig. 11).

However, such deformation requires a certain shear displacement to occur, and higher geogrid stiffness reduces the required displacement. Overall, an increase in geogrid stiffness promotes the passive resistance of transverse ribs. Consequently, maximizing the passive resistance of transverse ribs can be achieved by employing geogrids with higher rib stiffness.

7. Conclusions

In this study, three-dimensional DEM models were developed to simulate the direct shear tests investigating fundamental interaction mechanism of geogrid-aggregate interfaces. The DEM model was calibrated based on the experimental results. By analyzing the displacement field of particles, the local shear band at the geogrid-aggregate interface was identified, and the contact normal direction of particles within the shear band was determined. Different types of contacts were quantified to assess the evolution of each shear resistance component during the direct shear test of geogrid-aggregate interface. Furthermore, the influences of aperture-aggregate ratio (A_s/D_{50}) and geogrid stiffness ($J_{2\%}$) on the passive resistance of transverse ribs were investigated. The following conclusions can be drawn:

(1) Under direct shear of geogrid-aggregate interfaces, higher normal stresses prevent the upward extension of shear band while promoting its downward development. As the normal stress increases, the boundaries of the upper and lower shear bands shift downwards, while the total thickness of shear band remains relatively constant. This indicates that particles tend to be closely compressed and interlocked under high normal stress conditions.

(2) During the initial shearing stage, the frictional resistance between aggregates becomes

active, followed by the geogrid-aggregate interface frictional resistance. The development of passive resistance of transverse ribs exhibits a certain lag, particularly in the early stages of shearing. With increasing normal stress, each shear resistance component experiences significant growth, with the frictional resistance component of aggregates exhibiting the most pronounced increase.

(3) When the total shear resistance reaches its peak value under different normal stresses, the contribution of the passive resistance of transverse ribs ranges between 16.7% and 22.8%. The maximum contribution of the passive resistance of transverse ribs consistently occurs after the peak of total shear stress, reaching a maximum of 43.5%. Furthermore, the passive resistance of transverse ribs mobilizes shear strength at greater shear displacement levels than the other two shear resistance components.

(4) The relationship between the geogrid aperture size and aggregate size (A_s/D_{50}) has a limited impact on the geogrid-aggregate interface frictional resistance and the frictional resistance of aggregates. In contrast, the aperture-aggregate ratio plays a crucial role in enhancing the total shear strength by improving the passive resistance of transverse ribs. In this study, the maximum value of transverse rib passive resistance was increased by 110% and 41% at A_s/D_{50} = 2.38 compared to A_s/D_{50} = 1.67 and A_s/D_{50} = 3.33, respectively.

(5) Increasing the stiffness of geogrid has a minor influence on the frictional resistance of aggregate and geogrid-aggregate interface frictional resistance, but significantly affects the passive resistance of transverse ribs. Higher geogrid stiffness enables the mobilization of passive resistance from the transverse ribs under smaller relative displacements between the

geogrid and aggregates, thereby promoting the development of passive resistance of transverse ribs. Consequently, utilizing geogrids with higher rib stiffness maximizes the passive resistance of transverse ribs.

Acknowledgments

This research is supported by the National Natural Science Foundation of China (Grant No. 52278360 and 52078392) and the National Key R&D Program of China (Grant No. 2022YFC3080400). The authors gratefully acknowledge the financial supports.

Competing Interests Statement

The authors declare that they have no known competing financial interests or personal relationships that could have appeared to influence the work reported in this paper.

Data Availability Statement

Some or all data, models, or codes that support the findings of this study are available from the corresponding author upon reasonable request.

References

ASTM-D 5321. Standard test method for determining the coefficient of soil and geosynthetic or geosynthetic and geosynthetic friction by the direct shear method. West Conshohocken, PA, USA: ASTM International.

Abdelrahman, A.H., Ashmawy, A.K., Abdelmoniem, M., 2008. An Apparatus for Direct Shear, Pullout, and Uniaxial Testing of Geogrids. Geotechnical Testing Journal 31, 470-479.

Abdi, M.R., Mirzaeifar, H., 2017. Experimental and PIV evaluation of grain size and distribution on soil-geogrid interactions in pullout test. Soils and Foundations 57, 1045-1058.

Alfaro, M.C., Miura, N., Bergado, D.T., 1995. Soil-geogrid reinforcement interaction by pullout and direct shear tests. Geotechnical Testing Journal 18, 157-167.

Brown, S.F., Kwan, J., Thom, N.H., 2007. Identifying the key parameters that influence geogrid reinforcement of railway ballast. Geotextiles and Geomembranes 25, 326-335.

Cardile, G., Gioffre, D., Moraci, N., Calvarano, L.S., 2017. Modelling interference between the geogrid bearing members under pullout loading conditions. Geotextiles and Geomembranes 45, 169-177.

Chen, C., McDowell, G., Rui, R., 2018. Discrete element modelling of geogrids with square and triangular apertures. Geomechanics and Engineering 16, 495-501.

Chen, C., McDowell, G.R., Thom, N.H., 2012. Discrete element modelling of cyclic loads of geogrid-reinforced ballast under confined and unconfined conditions. Geotextiles and Geomembranes 35, 76-86.

Ezzein, F.M., Bathurst, R.J., 2014. A new approach to evaluate soil-geosynthetic interaction using a novel pullout test apparatus and transparent granular soil. Geotextiles and Geomembranes 42, 246-255.

Feng, G., Zhao, J., Wang, H., Li, Z., Fang, Z., Fan, W., Yang, P., Yang, X., 2022. Study of the internal re-breaking characteristics of broken limestone during compression. Powder Technology 396, 449-455.

Feng, S.-J., Liu, X., Chen, H.-X., Zhao, T., 2018. Micro-mechanical analysis of geomembrane-sand interactions using DEM. Computers and Geotechnics 94, 58-71.

Feng, S.J., Wang, Y.Q., 2023. DEM simulation of geogrid-aggregate interface shear behavior: Optimization of the aperture ratio considering the initial interlocking states. Computers and Geotechnics 154.

Ferellec, J.-F., McDowell, G.R., 2010. A method to model realistic particle shape and inertia in DEM. Granular Matter 12, 459-467.

Ferellec, J.F., McDowell, G.R., 2012. Modelling of ballast-geogrid interaction using the discrete-element method. Geosynthetics International 19, 470-479.

Ferreira, F.B., Vieira, C.S., Lopes, M.L., 2015. Direct shear behaviour of residual soil-geosynthetic interfaces - influence of soil moisture content, soil density and geosynthetic type. Geosynthetics International 22, 257-272.

Gao, G., Meguid, M.A., 2018. Effect of particle shape on the response of geogrid-reinforced systems: Insights from 3D discrete element analysis. Geotextiles and Geomembranes 46, 685-698.

Grabowski, A., Nitka, M., Tejchman, J., 2021. Comparative 3D DEM simulations of sand-structure interfaces with similarly shaped clumps versus spheres with contact moments. Acta Geotechnica 16, 3533-3554.

Indraratna, B., Hussaini, S.K.K., Vinod, J.S., 2013. The lateral displacement response of geogrid-reinforced ballast under cyclic loading. Geotextiles and Geomembranes 39, 20-29.

Jewell, R.A., Milligan, G.W.E., Sarsby, R.W., Dubois, D., 1985. Interaction between Soil and Geogrids. Proc., Conference on Polymer Grid Reinforcement, London, pp.18-29.

Jia, M., Zhu, W., Xu, C., 2021. Performance of a 33m high geogrid reinforced soil embankment without concrete panel. Geotextiles and Geomembranes 49, 122-129.

Jia, Y., Zhang, J., Chen, X., Miao, C., Zheng, Y., 2023. DEM study on shear behavior of geogrid-soil interfaces subjected to shear in different directions. Computers and Geotechnics 156.

Jiang, Y., Han, J., Parsons, R.L., Brennan, J.J., 2016. Field Instrumentation and Evaluation of Modular-Block MSE Walls with Secondary Geogrid Layers. Journal of Geotechnical and Geoenvironmental Engineering 142.

Jing, X.-Y., Zhou, W.-H., Zhu, H.-X., Yin, Z.-Y., Li, Y., 2018. Analysis of soil-structural interface behavior using three-dimensional DEM simulations. International Journal for Numerical and Analytical Methods in Geomechanics 42, 339-357.

Katagiri, J., 2019. A novel way to determine number of spheres in clump-type particle-shape approximation in discrete-element modelling. Geotechnique 69, 620-626.

Ke, H., Ma, P.C., Lan, J.W., Chen, Y.M., He, H.J., 2021. Field behaviors of a geogrid reinforced MSW slope in a high-food-waste-content MSW landfill: A case study. Geotextiles and Geomembranes 49, 430-441.

Liu, C.-N., Ho, Y.-H., Huang, J.-W., 2009a. Large scale direct shear tests of soil/PET-yarn geogrid interfaces. Geotextiles and Geomembranes 27, 19-30.

Liu, C.N., Zornberg, J.G., Chen, T.C., Ho, Y.H., Lin, B.H., 2009b. Behavior of Geogrid-Sand Interface in Direct Shear Mode. Journal of Geotechnical and Geoenvironmental Engineering 135, 1863-1871.

Liu, F.Y., Wang, P., Geng, X., Wang, J., Lin, X., 2016. Cyclic and post-cyclic behaviour from sand-geogrid interface large-scale direct shear tests. Geosynthetics International 23, 129-139.

Liu, F.Y., Ying, M.J., Yuan, G.H., Wang, J., Gao, Z.Y., Ni, J.F., 2021. Particle shape effects on the cyclic shear behaviour of the soil-geogrid interface. Geotextiles and Geomembranes 49, 991-1003.

Liu, F.Y., Zheng, Q.T., Wang, J., Fu, H.T., Gao, Z.Y., Ni, J.F., 2022. Effect of particle shape on shear behaviour of aggregate-geogrid interface under different aperture ratios. International Journal of Pavement Engineering 23, 2099-2109.

Liu, H.L., Ng, C.W.W., Fei, K., 2007. Performance of a geogrid-reinforced and pile-supported highway embankment over soft clay: Case study. Journal of Geotechnical and Geoenvironmental Engineering 133, 1483-1493.

Lopes, M.L., Ladeira, M., 1996. Influence of the confinement, soil density and displacement rate on soil-geogrid interaction. Geotextiles and Geomembranes 14, 543-554.

McDowell, G.R., Harireche, O., Konietzky, H., Brown, S.F., Thom, N.H., 2006. Discrete element modelling of geogrid-reinforced aggregates. Proceedings of the Institution of Civil Engineers-Geotechnical Engineering 159, 35-48.

Miao, C., Zheng, J., Zhang, R., Cui, L., 2017. DEM modeling of pullout behavior of geogrid reinforced ballast: The effect of particle shape. Computers and Geotechnics 81, 249-261.

Miao, C.X., Jia, Y.F., Zhang, J., Zhao, J.B., 2020. DEM simulation of the pullout behavior of geogrid-stabilized ballast with the optimization of the coordination between aperture size and particle diameter. Construction and Building Materials 255.

Mirtich, B., 1996. Fast and Accurate Computation of Polyhedral Mass Properties. Journal of Graphics Tools 1, 31-50.

Moraci, N., Gioffrè, D., 2006. A simple method to evaluate the pullout resistance of extruded geogrids embedded in a compacted granular soil. Geotextiles and Geomembranes 24, 116-128.

Ngo, N.T., Indraratna, B., Rujikiatkamjorn, C., 2014. DEM simulation of the behaviour of geogrid stabilised ballast fouled with coal. Computers and Geotechnics 55, 224-231.

Palmeira, E.M., 2009. Soil–geosynthetic interaction: Modelling and analysis. Geotextiles and Geomembranes 27, 368-390.

Palmeira, E.M., Milligan, G.W.E., 1989. Scale and other factors affecting the results of pull-out tests of grids buried in sand. Geotechnique 39, 511-524.

Peng, X., Zornberg, J.G., 2019. Evaluation of soil-geogrid interaction using transparent soil with laser illumination. Geosynthetics International 26, 206-221.

Rothenburg, L., Bathurst, R.J., 1989. Analytical study of induced anisotropy in idealized granular materials. Geotechnique 39, 601-614.

Stahl, M., Konietzky, H., te Kamp, L., Jas, H., 2014. Discrete element simulation of geogrid-stabilised soil. Acta Geotechnica 9, 1073-1084.

Sweta, K., Hussaini, S.K.K., 2018. Effect of shearing rate on the behavior of geogrid-reinforced railroad ballast under direct shear conditions. Geotextiles and Geomembranes 46, 251-256.

Tatlisoz, N., Edil, T.B., Benson, C.H., 1998. Interaction between Reinforcing Geosynthetics and Soil-Tire Chip Mixtures. Journal of Geotechnical and Geoenvironmental Engineering 124, 1109-1119.

Teixeira, S.H.C., Bueno, B.S., Zornberg, J.G., 2007. Pullout resistance of individual longitudinal and transverse geogrid ribs. Journal of Geotechnical and Geoenvironmental Engineering 133, 37-50.

Thornton, C., 2000. Numerical simulations of deviatoric shear deformation of granular media. Geotechnique 50, 43-53.

Tutumluer, E., Huang, H., Bian, X.C., 2012. Geogrid-Aggregate Interlock Mechanism Investigated through Aggregate Imaging-Based Discrete Element Modeling Approach. International Journal of Geomechanics 12, 391-398.

Wang, H.-L., Zhou, W.-H., Yin, Z.-Y., Jie, X.-X., 2019. Effect of Grain Size Distribution of Sandy Soil on Shearing Behaviors at Soil-Structure Interface. Journal of Materials in Civil Engineering 31.

Wang, J., Chi, S., Zhou, X., Shao, X., 2023. Experimental and numerical investigation of the size effect of rockfill particles on crushing strength. Granular Matter 25.

Wang, J., Liu, F.Y., Wang, P., Cai, Y.Q., 2016. Particle size effects on coarse soil-geogrid interface response in cyclic and post-cyclic direct shear tests. Geotextiles and Geomembranes 44, 854-861.

Wang, J., Ying, M., Liu, F., Yuan, G., Fu, H., 2021. Experimental investigation on the stress-dilatancy response of aggregate-geogrid interface using parameterized shapes. Construction and Building Materials 289.

Wang, P., Yin, Z.-Y., Zhou, W.-H., Chen, W.-b., 2022. Micro-mechanical analysis of soil-structure interface behavior under constant normal stiffness condition with DEM. Acta Geotechnica 17, 2711-2733.

Wang, P., Yin, Z.Y., 2022. Effect of particle breakage on the behavior of soil-structure interface under constant normal stiffness condition with DEM. Computers and Geotechnics 147.

Wang, Z.J., Jacobs, F., Ziegler, M., 2014. Visualization of load transfer behaviour between geogrid and sand using PFC2D. Geotextiles and Geomembranes 42, 83-90.

Yang, G., Liu, H., Lv, P., Zhang, B., 2012. Geogrid-reinforced lime-treated cohesive soil retaining wall: Case study and implications. Geotextiles and Geomembranes 35, 112-118.

Ying, M.J., Liu, F.Y., Wang, J., Wang, C.L., Li, M.F., 2021. Coupling effects of particle shape and cyclic shear history on shear properties of coarse-grained soil-geogrid interface. Transportation Geotechnics 27.

Zhang, J., Guo, W., Ji, M., Zhao, J., Xu, C., Zheng, Y., 2022. Field monitoring of vertical stress distribution in GRS-IBS with full-height rigid facings. Geosynthetics International 0, 1-12.

Zhou, J., Chen, J.F., Xue, J.F., Wang, J.Q., 2012. Micro-mechanism of the interaction between sand and geogrid transverse ribs. Geosynthetics International 19, 426-437.

Zhou, Y., Wang, H., Zhou, B., Li, J., 2018. DEM-aided direct shear testing of granular sands incorporating realistic particle shape. Granular Matter 20.

Table 1. Geogrid model parameters.

Parameter	Value
Density, ρ_g (kg/m^3)	972
Local damping coefficient, d_p	0.7
Friction coefficient, μ_g	0.43
Effective modulus, E^* (MPa)	6×10^2
Normal-to-shear stiffness ratio, κ^*	1
Longitudinal rib bond effective modulus, $\bar{E}^*$ (MPa)	8×10^2
Transverse rib bond effective modulus, $\bar{E}^*$ (MPa)	6×10^2
Bond normal-to-shear stiffness ratio, $\bar{\kappa}^*$	100
Bond radius multiplier, $\bar{r}_m$	1
Bond gap, $\bar{g}$ (m)	7.5×10^{-4}

Table 2. Aggregate particle model parameters.

Parameter	Value
Density, ρ_a (kg/m^3)	2650
Local damping coefficient, d_p	0.7
Friction coefficient, μ_a	0.55
Effective modulus, E^* (MPa)	2×10^3
Normal-to-shear stiffness ratio, κ^*	1

Table 3. Geogrid-aggregate contact parameters.

Parameter	Value
Friction coefficient, μ_s	0.43
Effective modulus, E^* (MPa)	1.3×10^3
Normal-to-shear stiffness ratio, K^*	1

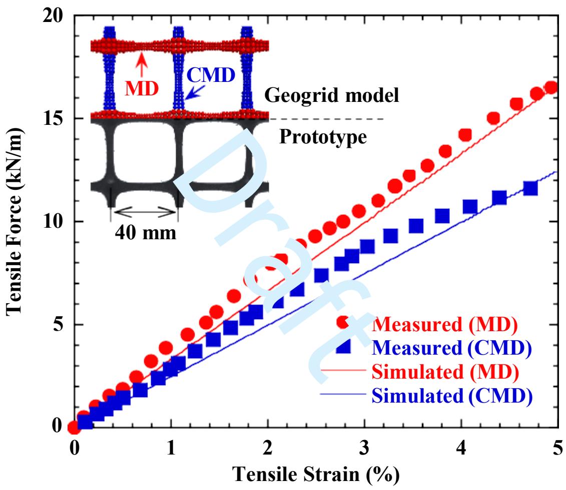

Fig. 1. Comparison of tensile test results between experiments and DEM simulations.

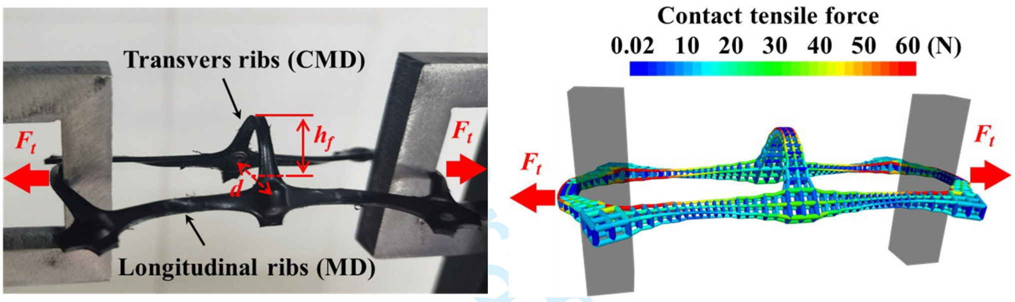

(a) (b)

Fig. 2. Comparison of two-aperture extension test results between experiment and DEM simulation: (a) experiment; (b) DEM simulation.

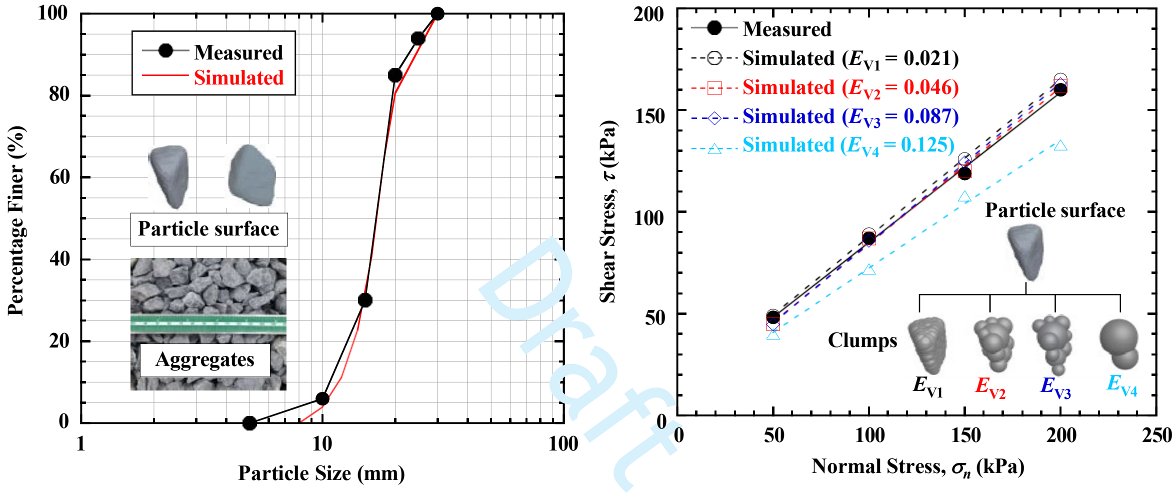

(a) (b)

Fig. 3. Comparison between experiments and DEM simulations: (a) particle size distribution; (b) shear strength.

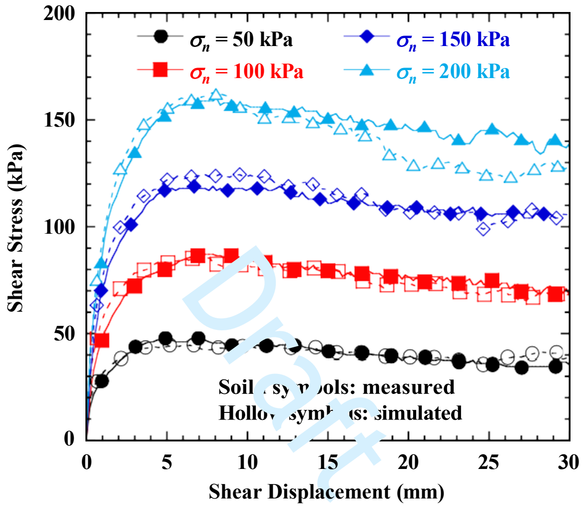

Fig. 4. Comparison of direct shear test results between experiments and DEM simulations.

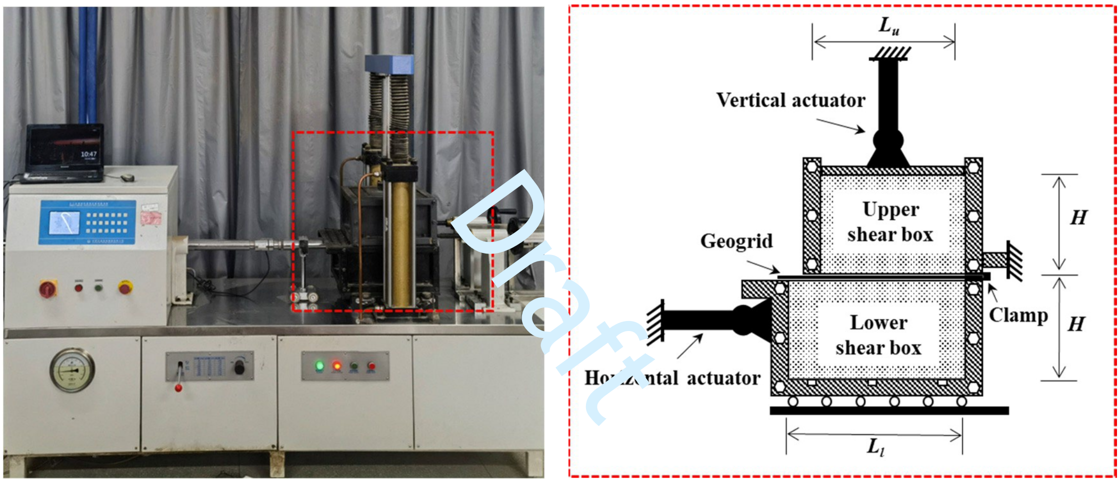

Fig. 5. Apparatus for geogrid-aggregate interface direct shear test.

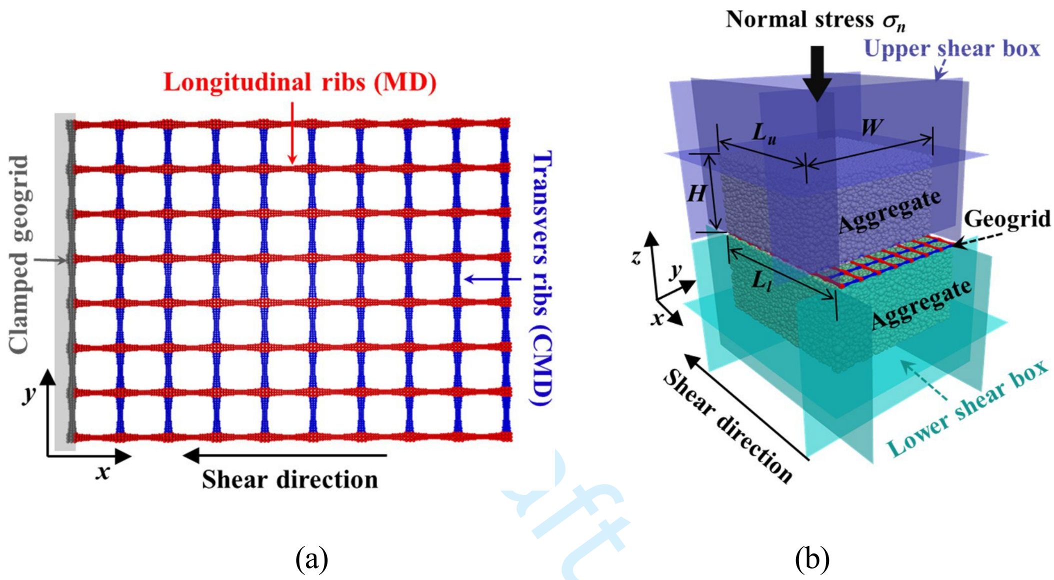

Fig. 6. DEM model of direct shear test: (a) geogrid model; (b) geogrid-aggregate interface shear model.

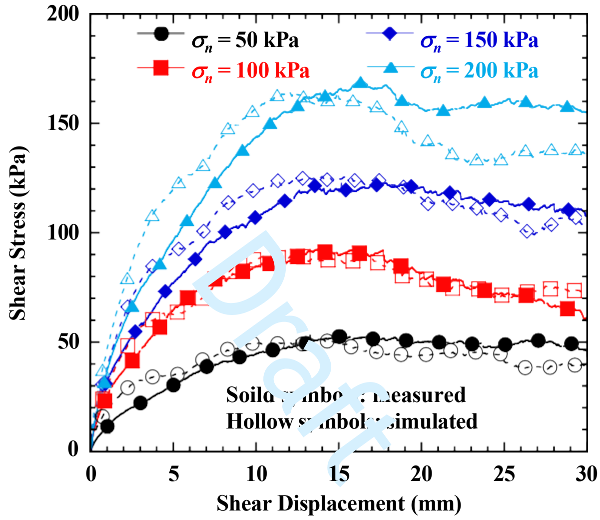

Fig. 7. Comparison of interface direct shear test results between experiments and DEM simulations.

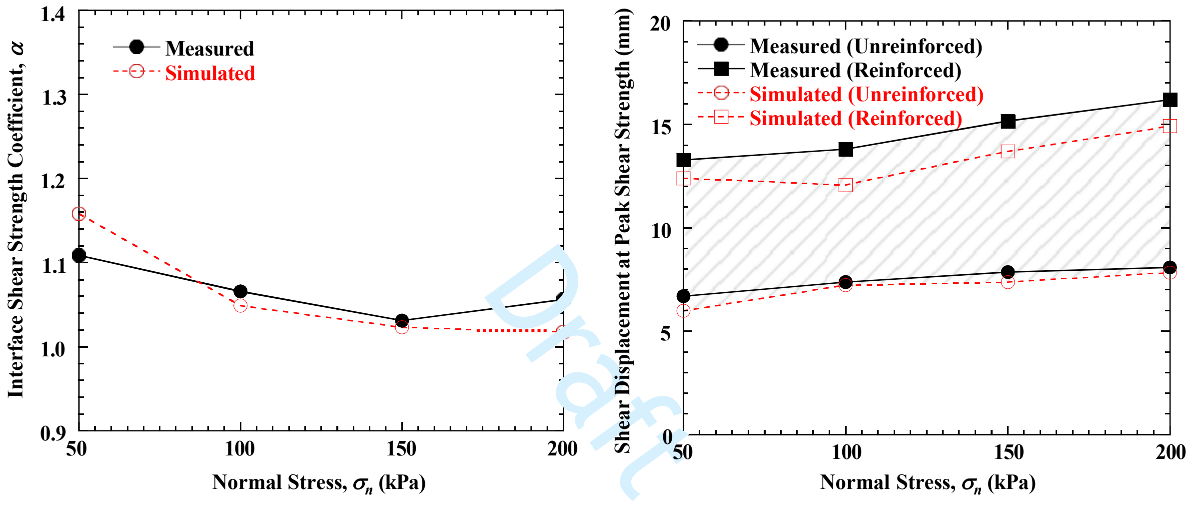

(a) (b)

Fig. 8. Comparison of experiments and DEM simulations: (a) interface shear strength coefficient; (b) shear displacement at peak shear strength.

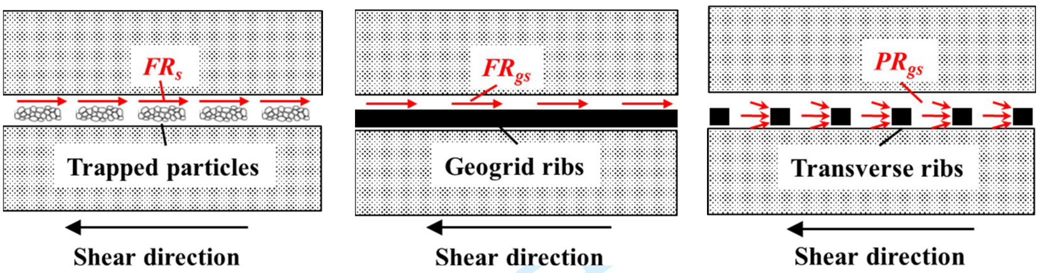

Fig. 9. Shear resistance components in direct shear test.

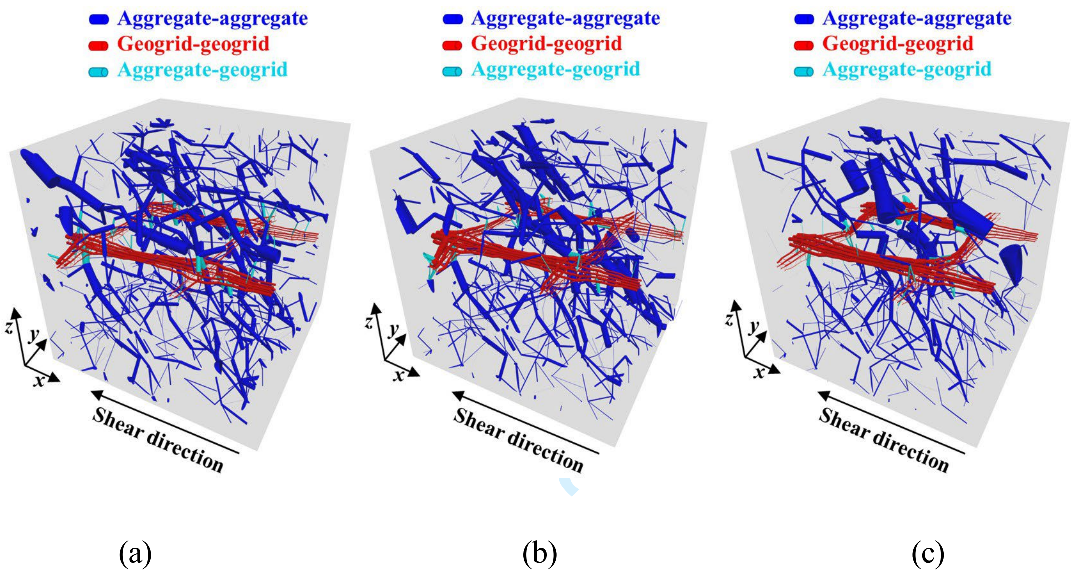

Fig. 10. Contact force distribution mobilized in an aperture of geogrid: (a) at shear displacement of 9 mm; (b) at shear displacement of 18 mm; (c) at shear displacement of 27 mm.

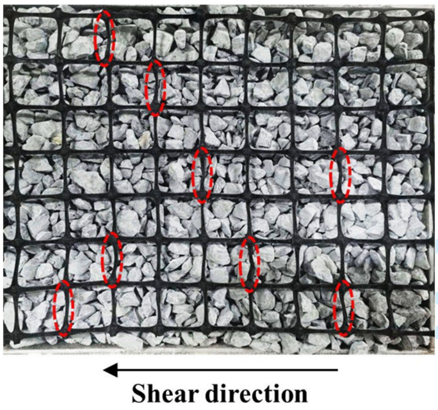

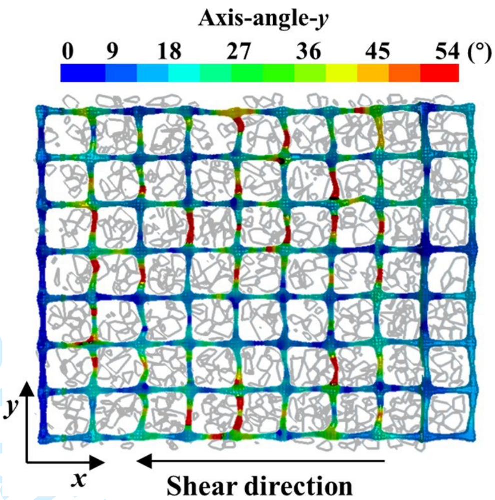

Fig. 11. Comparison of geogrid deformations after shear between experiment and DEM simulation under σ_n = 50 kPa: (a) experiment; (b) DEM simulation.

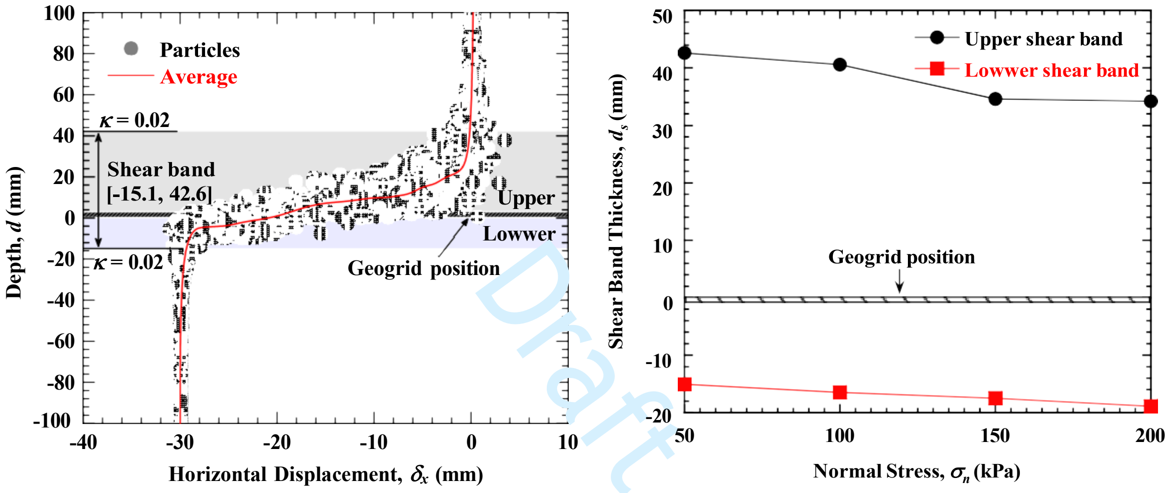

(a) (b)

Fig. 12. Shear band distribution: (a) aggregate particle displacement distribution; (b) shear band thickness.

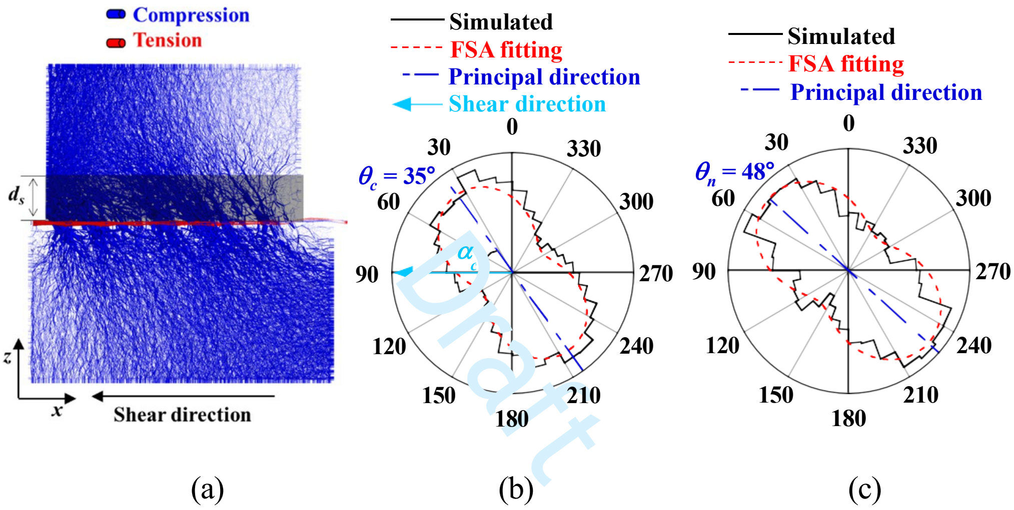

Fig. 13. Contact force chains: (a) contact distribution at peak shear strength; (b) contact normal direction fitting; (c) normal contact force direction fitting.

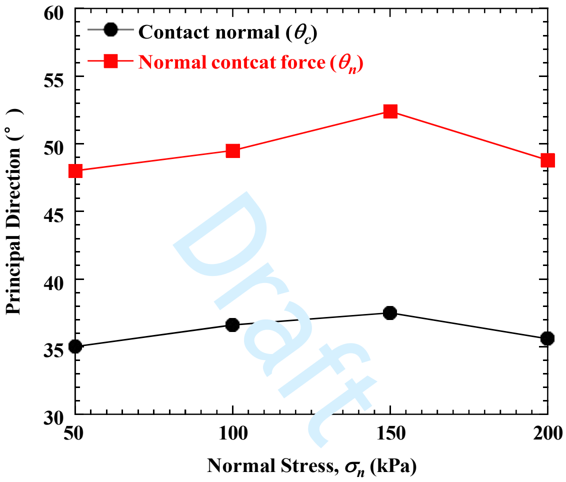

Fig. 14. Principal direction of contact normal and normal contact force.

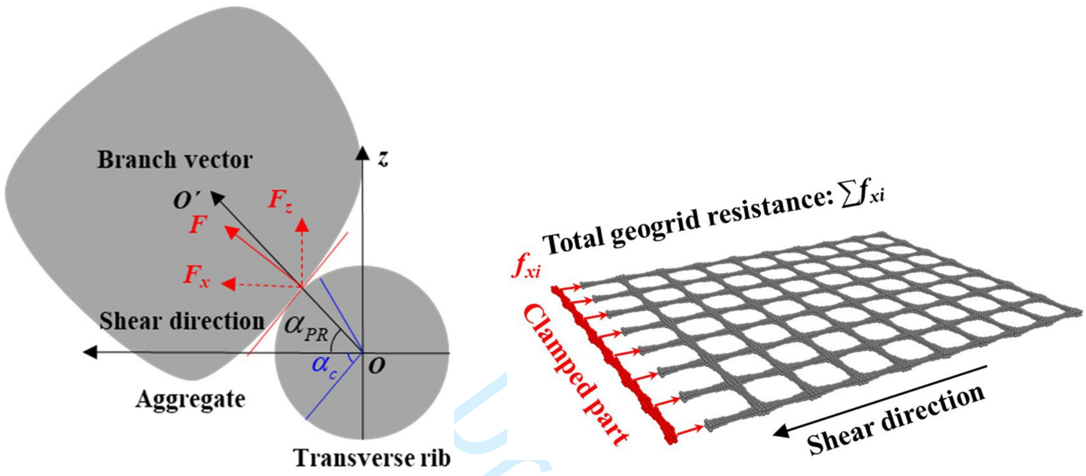

(a) (b)

Fig. 15. Identification of contact forces contributing to shear resistance: (a) contacts contributing to transverse rib passive resistance; (b) contacts contributing to total geogrid resistance.

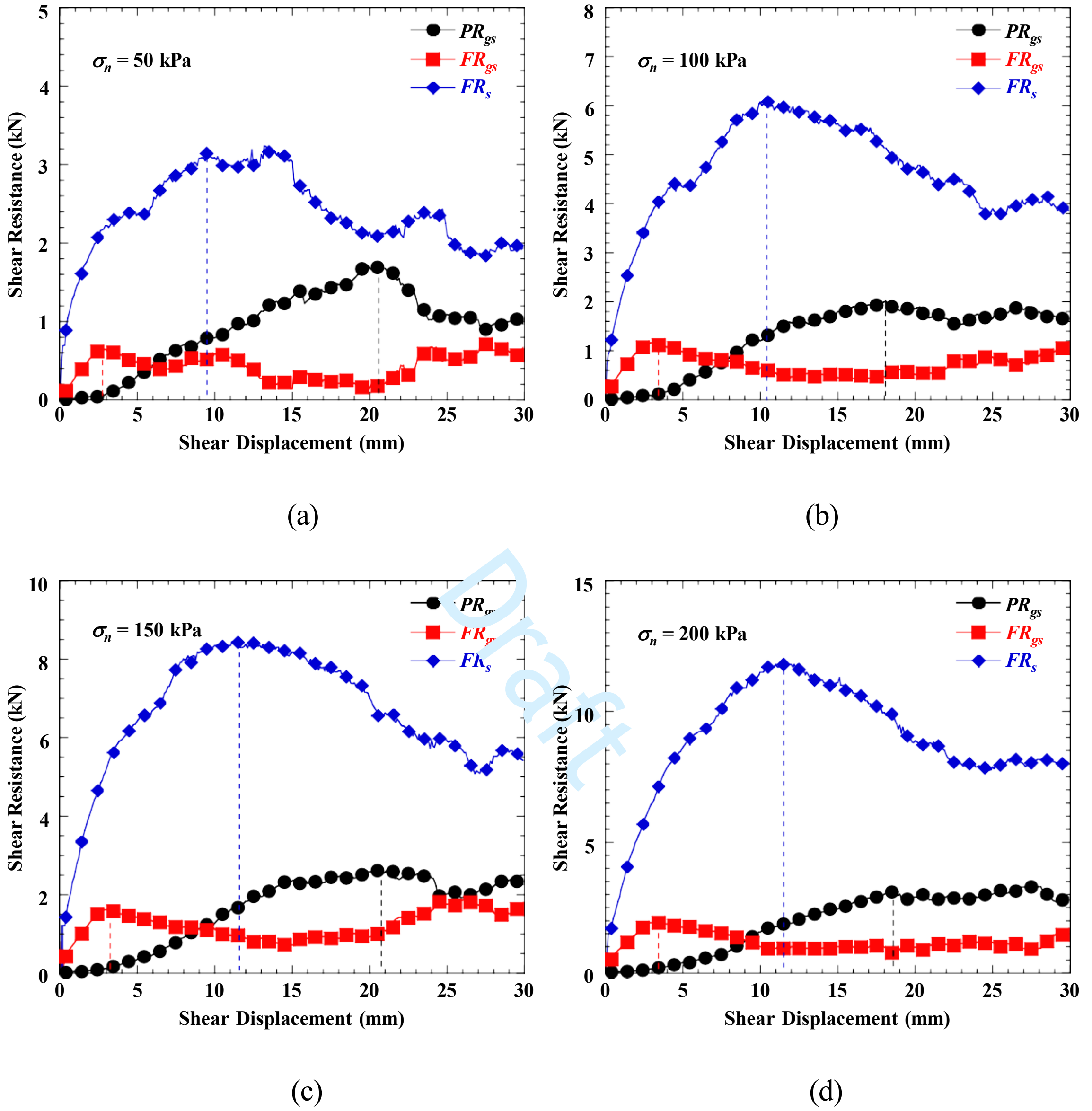

Fig. 16. Shear resistance component evolution under different normal stresses: (a) σ_n = 50 kPa; (b) σ_n = 100 kPa; (c) σ_n = 150 kPa; (d) σ_n = 200 kPa.

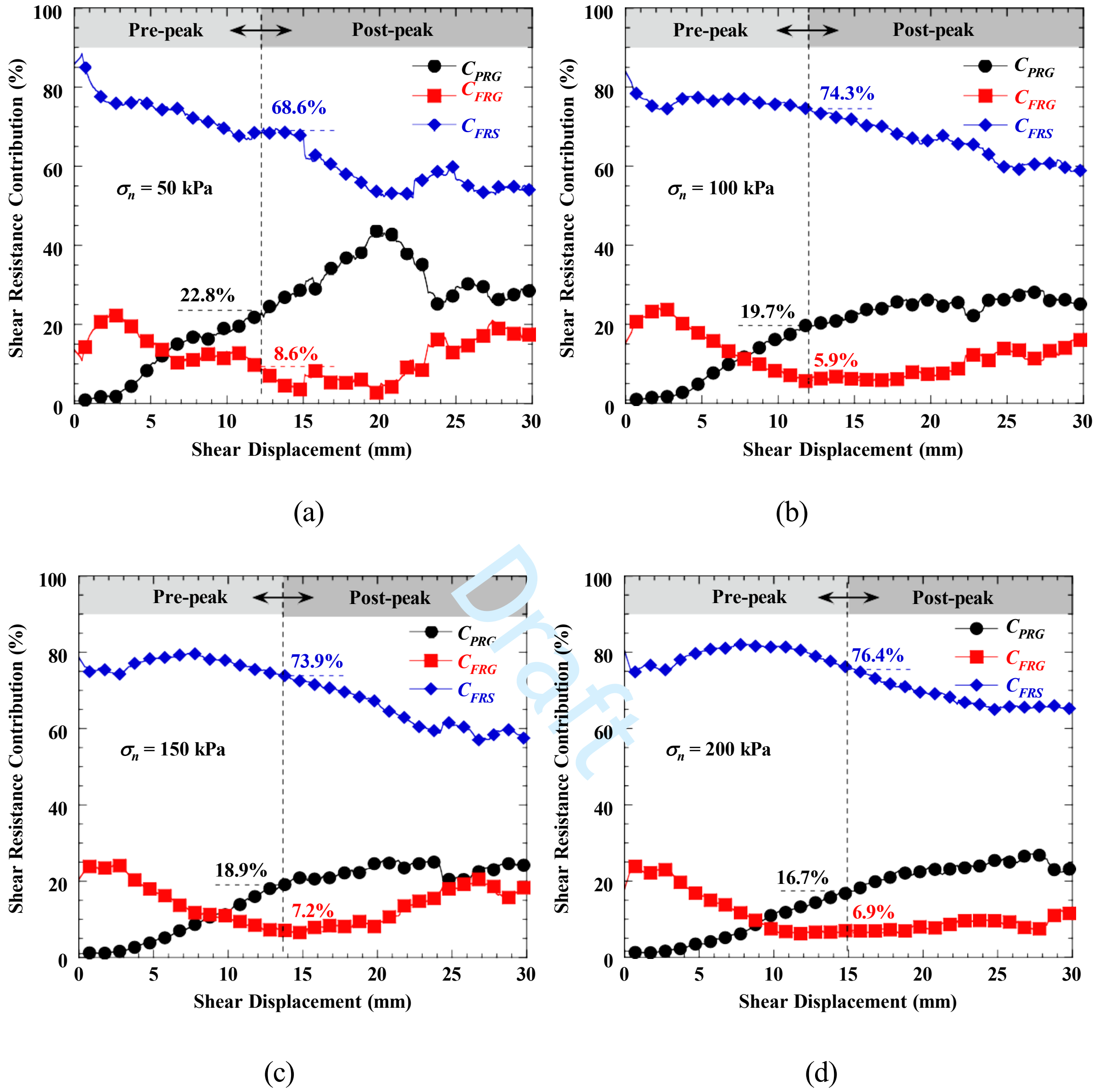

Fig. 17. Shear resistance contribution under different normal stresses: (a) σ_n = 50 kPa; (b) σ_n = 100 kPa; (c) σ_n = 150 kPa; (d) σ_n = 200 kPa.

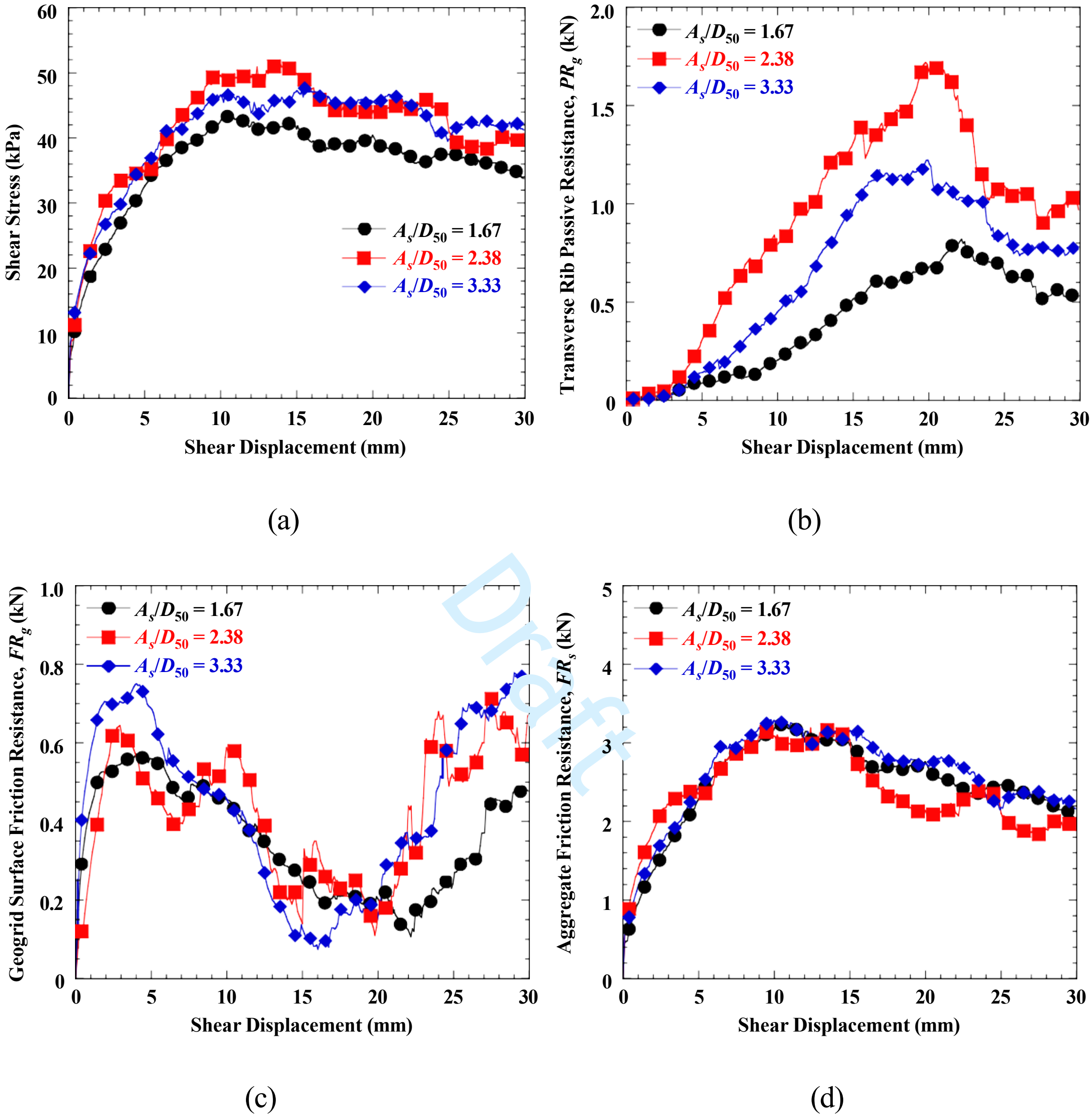

Fig. 18. Influence of aperture-aggregate ratio: (a) total shear stress; (b) transverse rib passive resistance; (c) geogrid-aggregate interface frictional resistance; (d) frictional resistance of aggregate.

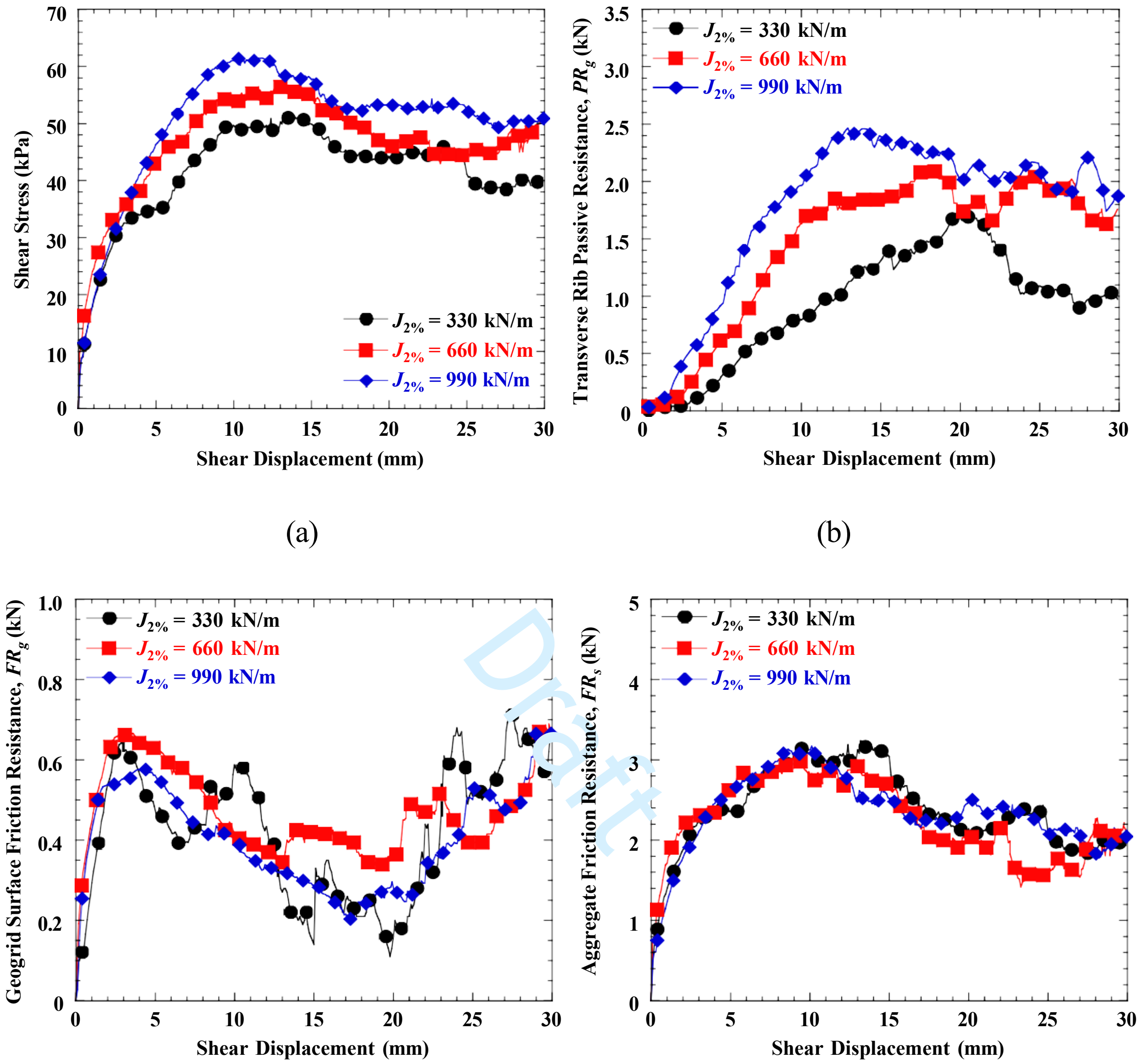
Shear Stress (kPa)
Shear Displacement (mm)
$J_{2\%}$ = 330 kN/m
$J_{2\%}$ = 660 kN/m
$J_{2\%}$ = 990 kN/m
(a)
Transverse Rib Passive Resistance, PR_g (kN)
Shear Displacement (mm)
$J_{2\%}$ = 330 kN/m
$J_{2\%}$ = 660 kN/m
$J_{2\%}$ = 990 kN/m
(b)
Geogrid Surface Friction Resistance, FR_g (kN)
Shear Displacement (mm)
$J_{2\%}$ = 330 kN/m
$J_{2\%}$ = 660 kN/m
$J_{2\%}$ = 990 kN/m
Aggregate Friction Resistance, FR_s (kN)
Shear Displacement (mm)
$J_{2\%}$ = 330 kN/m
$J_{2\%}$ = 660 kN/m
$J_{2\%}$ = 990 kN/m

(c) (d)

Fig. 19. Influence of geogrid rib stiffness: (a) total shear stress; (b) transverse rib passive resistance; (c) geogrid-aggregate interface frictional resistance; (d) frictional resistance of aggregate.